Laser Absorption Spectroscopy Measurements of Post-Shock Non-Equilibrium Species in the NASA Ames Electric Arc Shock Tube

Efaine Chang*, Jesse W. Streicher ‡, Christopher L. Strand §, Ronald K. Hanson ¶
Stanford University, Stanford, California 94305, USA

Augustin C. Tibère-Inglesse‖
NASA Postdoctoral Fellow at NASA Ames Research Center, Mountain View, CA, 94035, USA

Brett A. Cruden**
AMA, Inc., at NASA Ames Research Center, Moffett Field, California 94035, USA

The NASA Ames Electric Arc Shock Tube (EAST) is a unique facility capable of generating high enthalpy, shock-heated impulse gas flows representative of the kinetic and radiative conditions encountered by atmospheric entry vehicles. The facility maintains a successful history with emission spectroscopy, providing measurements of absolute radiance upon which various validation studies are anchored. The central objective of this work is to develop a comprehensive tunable diode laser absorption spectroscopy (TDLAS) sensing capability to provide complementary experimental insights to existing emission techniques. More specifically, a fast-scanning TDLAS-based diagnostic targeting the cyano radical (CN) in the near-infrared (near-IR) near 926.6 nm is employed in mixtures of 2.2% CH_4 in N_2 by mole for a sweep of incident shock velocities ranging 3.0-5.5 km/s and fill pressures 0.3-1.15 Torr. Laser scan rates up to 500 kHz probe multiple absorption features to provide quantitative measurements of temperature and species number density profiles behind the incident shock. In all instances, the temperature trend is consistent between emission-inferred and TDLAS-inferred measurements. However, at the lower-velocity conditions, there is an appreciable offset between the Data Parallel Line Relaxation Code (DPLR) simulation and experimental measurements. A similar behavior is observed in number density profiles, with emission measurements providing inferences of the CN(B) and CN(A) state, while TDLAS measurements provide an additional inference of the CN(X) state. In the fast-scanned experiments, measurement inferred number densities suggest a much faster production of CN at early times than captured by the model. This discrepancy motivates ongoing, additional spectroscopic and kinetics CN experiments to resolve the accuracy of modeling assumptions.

I. Nomenclature

A_i	=	integrated absorbance of transition i, cm^{-1}
A_{21}	=	Einstein A coefficient, s^{-1}
c	=	speed of light, cm s^{-1}
E_i"	=	lower-state energy of transition i, cm^{-1}
$FWHM$	=	full width at half maximum of an absorption feature, cm^{-1}
g	=	degeneracy
h	=	Planck constant, J s

*Graduate Research Assistant, Department of Aeronautics and Astronautics. AIAA Student Member.
‡Research Scientist, Department of Mechanical Engineering. AIAA Member.
§Senior Research Engineer, Department of Mechanical Engineering. AIAA Member.
¶Clarence J. and Patricia R. Woodward Professor of Mechanical Engineering, Department of Mechanical Engineering. AIAA Fellow.
‖NASA Postdoctoral Program Fellow at NASA Ames Research Center.
**Senior Research Scientist, Aerothermodynamics Branch. AIAA Associate Fellow.

I_o = incident intensity
I_t = transmitted intensity
J'' = lower state rotational quantum number
k_B = Boltzmann constant, J K^{-1}
L = path length, cm
M = molecular weight of absorbing species, g/mol
n = number density, mol cm^{-3}
P = pressure, atm
Q = partition function
S_i = linestrength of transition i, cm^{-2} atm^{-1}
T_{trans} = translational temperature, K
T_{rot} = rotational temperature, K
T_{vib} = vibrational temperature, K
U_{is} = incident shock velocity, km/s
v'' = lower state vibrational quantum number
X = mole fraction
α = absorbance
$\nu_{0,i}$ = center wavenumber of transition i, cm^{-1}
$\Delta\nu_C$ = collisional FWHM, cm^{-1}
$\Delta\nu_D$ = Doppler FWHM, cm^{-1}
ϕ_i = lineshape function of transition i, cm

II. Introduction

Accurately simulating planetary entry conditions requires a robust understanding of complex molecular physics including internal energy excitation, dissociation, ionization, radiative emission, and chemical kinetics [1]-[3]. The validation of non-equilibrium models requires a characterization of the atmospheric entry shock layer conditions beyond surface measurements, which may not fully capture nonequilibrium in the core of the flow [4]-[6]. Such conditions may be produced in the NASA Ames Electric Arc Shock Tube (EAST) and similar facilities. Spectroscopic techniques have the potential to provide non-intrusive species and state-specific information from which additional flow properties such as temperature, composition, and flow velocity may be discerned. The EAST facility currently employs emission-based diagnostics, for which the interpretation relies on excitation rates from non-Boltzmann modeling and spectroscopic constants that may carry significant uncertainty for certain species, including the cyano radical (CN). In contrast, absorption-based diagnostics provide a direct probing of quantum-state-specific populations. This work leverages laser absorption spectroscopy (LAS) in order to provide time-resolved measurements of species concentrations, state populations, and gas temperatures to characterize the flows generated in the EAST facility. These measurements are then compared to Data Parallel Line Relaxation Code (DPLR) simulations for validating kinetic and radiation models employed in the design of thermal protection systems.

CN is a strong radiator that forms via chemical reactions of the CH_4/N_2 in the Titan atmosphere, CO_2/N_2 in the Martian atmosphere, and through ablation processes [7], [8], [9]. The presence of CN at elevated temperatures allows for measurements of gas properties using TDLAS. The CN spectrum may be described by two systems, the Violet system ($B^2\Sigma^+ \leftarrow X^2\Sigma^+$, 350-430 nm) accessed via ultraviolet (UV) and the Red system ($A^2\Pi \leftarrow X^2\Sigma^+$, 500-1300 nm) accessed via near-IR. Although the Violet system is orders of magnitude stronger in absorption, the form factor of UV laser systems is much larger and less portable. Meanwhile, lasers in the IR can be readily transported and integrated, accessing lines with high signal-to-noise (SNR) in the CN Red system. Hence, this work focuses on the CN Red system for scanned speciation and thermometry. Furthermore, a lack of literature on CN spectroscopy, particularly for the Red system, presents an exciting opportunity for LAS-based experimental data.

III. Theoretical Background

A. Laser absorption spectroscopy

Laser absorption spectroscopy is a well-established technique for non-intrusive flow diagnostics [10]. LAS leverages the attenuation of light by atomic and molecular transitions to infer properties of the absorbing gas. The Beer-Lambert

relation (Eqn. 1) expresses the quantitative relationship between the fractional transmission of monochromatic light and physical gas properties.

$$\alpha_\nu = -\ln\left(\frac{I_t}{I_0}\right) = \sum_i P X_{\text{abs}} S_i(T) \phi_i(\nu) L \tag{1}$$

For a uniform path-length, the spectral absorbance α_ν at frequency ν can be calculated from the fractional transmission of light I_t/I_0. In general, the absorption process is a function of fundamental, quantum-mechanical properties of the absorbing species and the number density in the absorbing state as in Eq. 4. However, for engineering applications, absorption can also be expressed in terms of thermodynamic quantities of interest. Absorbance may then be related to the pressure P, optical path length L, mole fraction of the absorbing species X_{abs}, temperature-dependent linestrength of the quantum transition $S_i(T)$, and $\phi_i(\nu)$ the lineshape function of the ith quantum transition. Then, with an appropriate model of spectroscopic parameters, knowledge of experimental parameters, and judicious selection of probed transitions, it is possible to obtain information on the energy distribution in the flow field.

By spectrally tuning the laser light across the absorbing bandwidth of a quantum transition, the measured absorbance can be frequency integrated to eliminate the dependence on the lineshape function (Eqn. 2).

$$A_i = P X_{\text{abs}} S_i(T) L \tag{2}$$

The integrated absorbance A_i is inferred by fitting a Voigt profile to absorbance data to capture both Doppler ($\Delta\nu_D$) and collisional ($\Delta\nu_C$) broadening.

Given a single transition, a Doppler-temperature may then be extracted from the Doppler width according to Eqn. 3.

$$\Delta\nu_D = 7.1623 \times 10^{-7} \nu_0 \sqrt{\frac{T}{M}} \tag{3}$$

Given multiple transitions, the mode-specific temperatures (rotational and vibrational) can be obtained by fitting Eqn. 4, wherein the line strength of Eqn. 2 is expressed as a function of the transition-specific Einstein A coefficient, state degeneracies, and additional molecular properties [11]. This formulation better emphasizes the dependence of absorption on the number density in the absorbing state.

$$A_i = L \frac{n_1 A_{21,i} g_{2,i}}{8\pi c \nu_{0,i}^2 g_{1,i}} \left(1 - \exp\left(-\frac{\nu_{0,i}}{k_B T}\right)\right) \tag{4}$$

Substituting in the equation of state and Boltzmann distribution, Eqn. 4 may be rearranged as

$$A_i = n_j L \frac{A_{21,i} g_{2,i}}{8\pi c \nu_{0,i}^2 Q_j(T)} \exp\left(-\frac{E_{1,i}}{k_B T}\right) \left(1 - \exp\left(-\frac{\nu_{0,i}}{k_B T}\right)\right) \tag{5}$$

The Einstein coefficient of spontaneous emission $A_{21,i}$, upper-state degeneracy $g_{2,i}$, vacuum line center $\nu_{0,i}$, and lower state energies $E_{1,i}$ are obtained from the HITEMP database [12]. The total partition function Q_j is calculated by summing contributions from all rotational and vibrational levels obtained from the ExoMol trihybrid line list [13]. The measured absorbance data is, subsequently, fit to Eqn. 5 via a weighted least-squares approach for all transitions i simultaneously. The number density n_j and temperature T can be captured as the free variables when a sufficient number of transitions are probed.

B. Line Selection

To provide a sensitive speciation diagnostic, it is desirable to optimize the line selection for transition strength and isolation from interfering species. Fig. 1 simulates the CN absorbance spectra of various lower vibrational bands at a representative test condition.

In this work, six features near 926.6 nm in the CN Red system are selected for strong absorbance, as predicted by Stanford-developed spectroscopic models, and for the ability to use a single laser to capture multiple features in a single scan at high scan rates, lowering the uncertainty in fits and inferred quantities. Table 1 provides transition information for each feature and Figure 2 present the simulated absorbance of the selected wavelengths at equilibrium for various incident shock velocities, with post-incident shock conditions predicted from the chemistry shock calculator, FROSH [14].

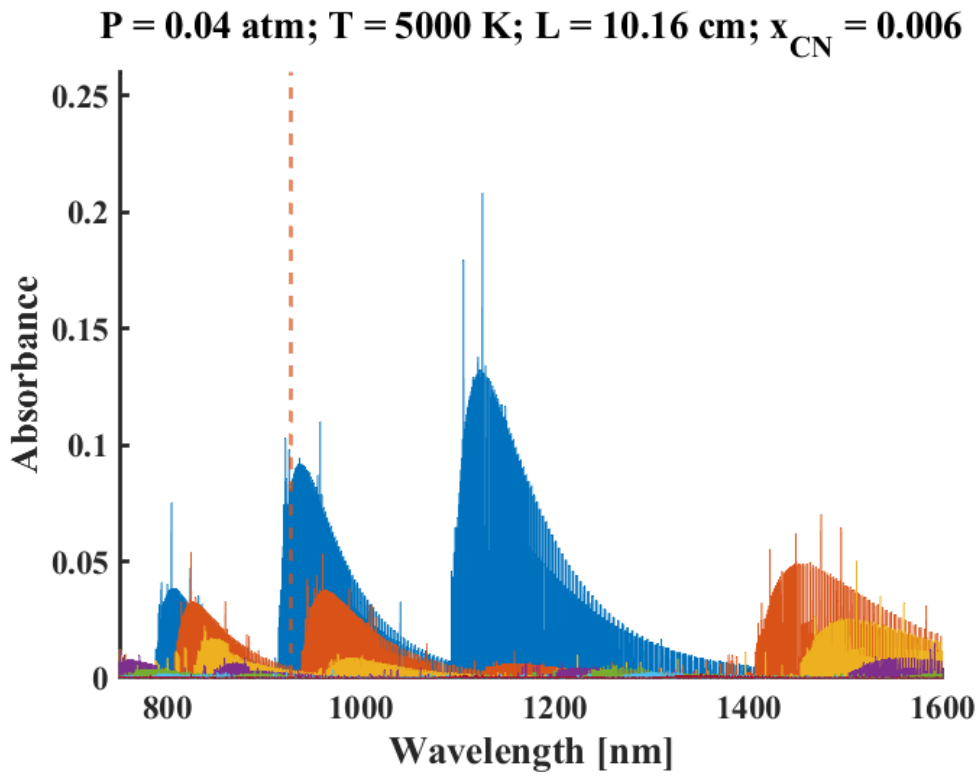

Fig. 1 Simulated absorbance of CN vibrational bands at a sample experimental condition. Dashed red line marks absoprtion transitions considered in this work.

$\nu_0[cm^{-1}]$	$\nu_0[nm]$	v"	v'	J"	Branch
10792.791	926.54	0	1	21.5	R12
10792.628	926.56	0	1	22.5	Q11
10792.142	926.60	0	1	14.5	Q12
10792.033	926.61	0	1	15.5	P11
10791.627	926.64	0	1	24.5	Q22
10791.449	926.66	0	1	25.5	P21

Table 1 Transition information for selected CN lines.

IV. Experimental Setup

Broadly, the EAST facility can be described as a closed tube partitioned by a diaphragm into a low-pressure driven section and high-pressure arc-driver section. The driven section is filled with the test gas, and an electric current is discharged through the driver gas, typically hydrogen or helium, leading to a rapid rise in the temperature and pressure in the driver section. In this work, a mixture of helium and argon is used to achieve lower velocities. The diaphragm is ruptured by the pressure differential, generating a shock wave which propagates down the tube, heating and pressurizing the test gas. The test section is located near the end of the driven section, instrumented with ports and windows for time-of-arrival sensors and emission spectrometers. The incident shock then traverses through a dump tube into a large, low-pressure dump tank. More detailed description of the facility may be found in [15]. Test times are defined as the interval between the passage of the incident shock and arrival of the contact surface between the driven and driver gases, and range from 1 μs to the order of 100 μs, shortening with decreasing pressure and increasing shock velocity.

In this work, test conditions are generated in the 4-inch diameter High Velocity Shock Tube (HVST) at the EAST facility. Here, the driven section is a 9.5 m long aluminum section that is filled with a Titan atmosphere mixture of 2.2% CH_4 in N_2 by mole. The start of the test section is located 7.5 m downstream of the diaphragm, with the

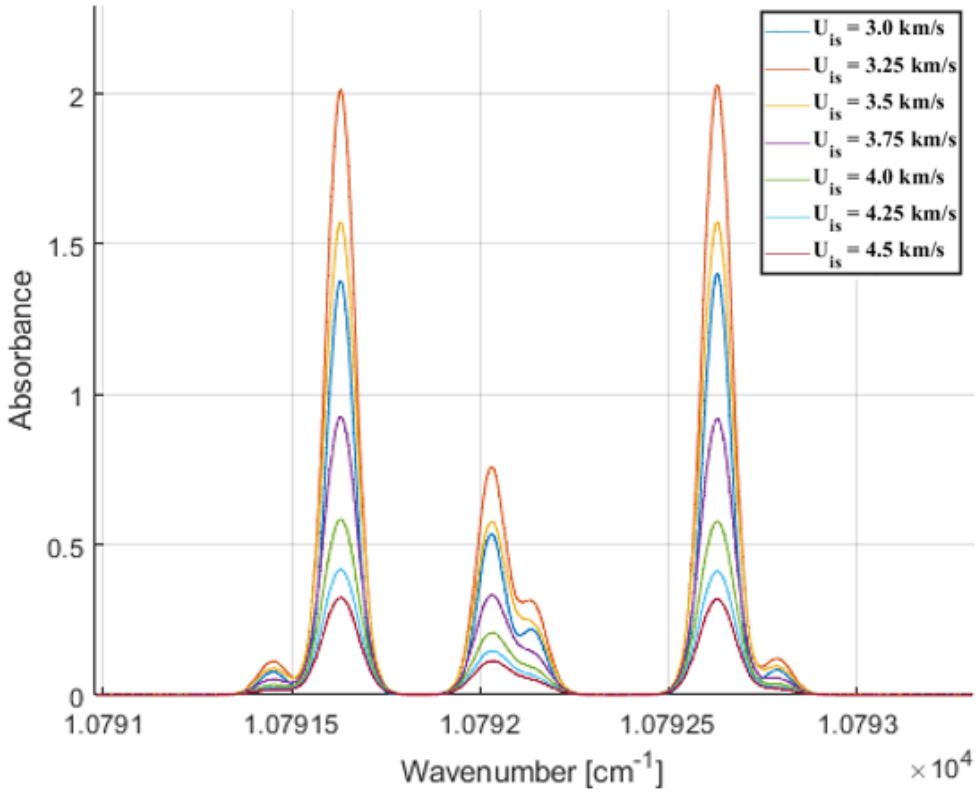

Fig. 2 Simulated absorbance of the selected wavelengths at equilibrium for various incident shock velocities. Post-incident shock conditions predicted according to FROSH.

TDLAS sensor located approximately 7.9 m downstream of the diaphragm. Time-of-arrival sensors are placed 3.175 cm apart for high-resolution velocity measurements, and a 13.4-inch slot window is present for shock wave imaging and spatially-resolved emission measurements. The initial temperature and pressure are calculated from the incident shock velocity using FROSH. The shock tube environment and associated equipment allow for controlled, repeatable experimental conditions.

Figure 3 provides a diagram of the sensor architecture for the Titan entry measurements and integration with the EAST facility. The laser is a distributed feedback (DFB) Nanoplus laser, covering wavelengths around 926.6 nm for access to the CN Red system. The laser scans over a narrow range of wavelengths to probe the lineshape and linestrength of an absorbing spectroscopic feature. For spectral tuning, the DFB is modulated at high-frequency scan-rates up to 500 kHz with a sinusoidal waveform (Fig. 4). Since absorption is probed on the upscan and downscan, measurements are obtained at up to 1 MHz rates. The optical alignment is optimized to mitigate non-ideal effects including density steering and emission, and fiber-coupled for ease of use and laser safety. The fiber optics direct the laser beams across the tube, through 2° wedged sapphire windows, and are then collected by high-bandwidth Thorlabs PDA10A2 detectors with 0.8 mm^2 active area. A lens, spectral filter, and neutral density (ND) filters are inserted in the detector cage system to optimize signal. Detector signals are recorded at a rate of 3 GS/s. A 9.97 cm YAG-etalon is used to obtain a time to wavenumber space conversion as in Figure 3. In combination, this set-up allows for high-SNR, high time-resolution measurements.

V. Results

The purpose of the Titan test series was to obtain data that can be applied to off-stagnation point radiative heating for the Dragonfly mission, providing benchmark data for the Shock Tube Informed Bias (STIB) model [16]. Incident shock velocities ranged from 3.0-5.5 km/s and fill pressures from 0.3-1.15 Torr. TDLAS scan rates were varied from 50

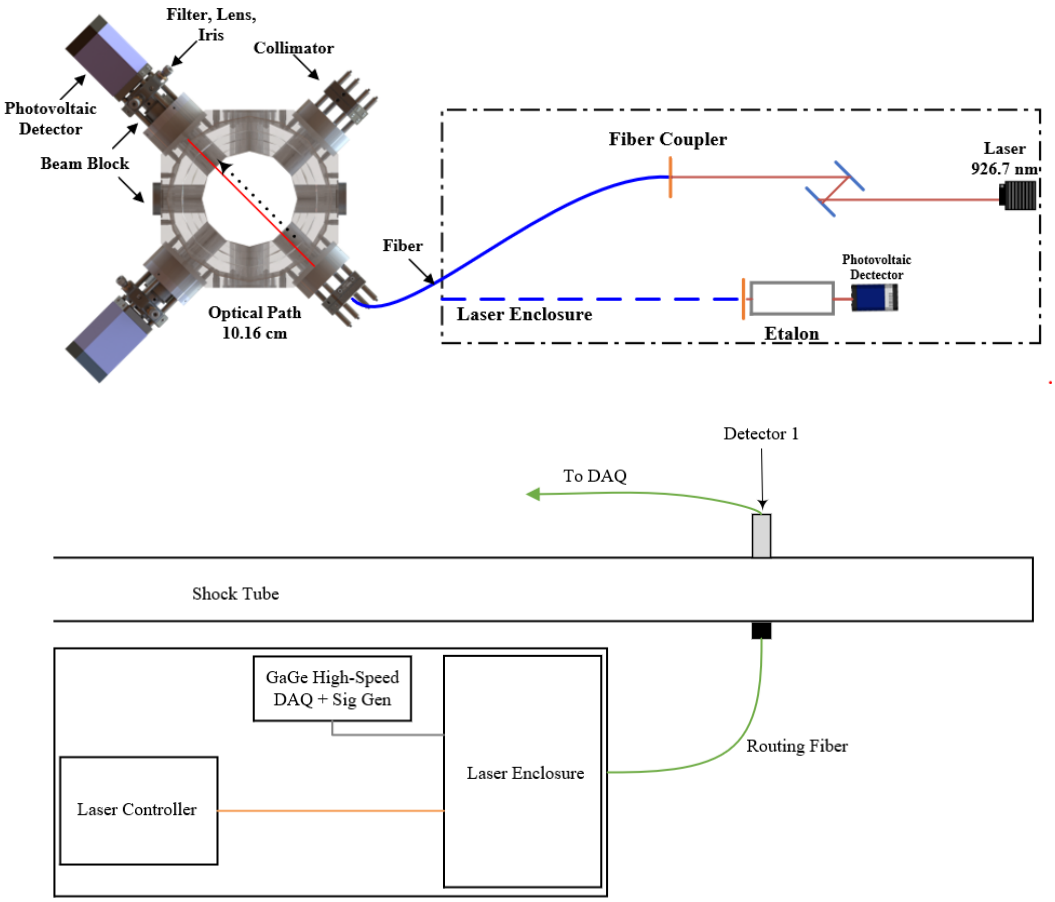

Fig. 3 (Top) Sensor diagram showing enclosure and pitch/catch system on EAST facility. (Bottom) Laser system layout and integration with EAST.

kHz to 500 kHz. For a given laser, the laser scan rate is a balance between temporal resolution and spectral scan range, directly proportional to and inversely proportional to scan rate, respectively. Hence, due to a lack of literature on CN spectroscopy, particularly for the Red system, the slower scan rates are critical for capturing a larger scan range for which to anchor unique CN absorbance features to in wavenumber space. Once confirmed, the higher scan rates are required for temporal resolution.

As outlined in III.A, the raw absorbance data is fit with a Voigt profile (Fig. 5) to obtain a time-varying integrated area. In this work, the limited range of v" and J" encompassed by the scanned features inhibit diagnostic sensitivity to vibrational and rotational energy distributions, respectively, and corresponding temperatures. Restricted by the temperature insensitivity of the accessible lines then, a Doppler temperature is extracted in place of state-specific temperatures according to Eq. 3. The integrated absorbance histories are then used to infer number density time-histories according to Eq. 5.

The temperature and number density time-histories for a representative condition at a 50 kHz scan rate are provided in Fig. 6. This slowed scan rate favors a larger scan range to anchor observed features rather than high temporal resolution. Therefore, only a few scans are captured within the test time, obviating quantitative inferences from subsequent scans. The available data points are plotted against emission-based temperature inferences and the DPLR prediction for reference, appearing to track well within the test time. DPLR predictions are extracted from the stagnation line of a flow around a sphere simulation, utilizing the corrected Gökçen model for Titan atmosphere kinetics [17], [18], [19]. Note that while the experimental temperatures agree within 10%, there is a considerable offset of approximately 20% with DPLR. Emission inferences of the CN(B) and CN(A) states, TDLAS inferences of the CN(X) population, and DPLR predictions of CN(Total) are also provided in Fig. 6. The relative population of each state is as expected, with

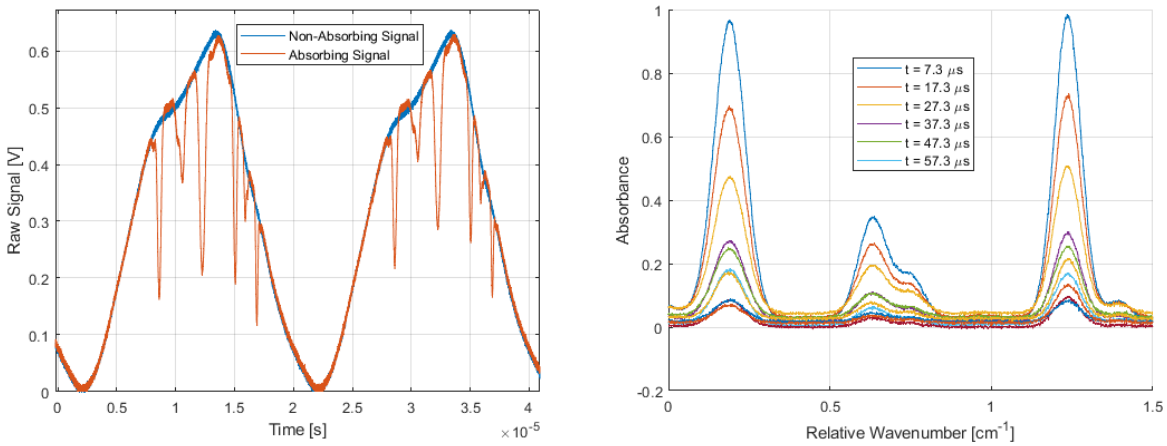

Fig. 4 This data corresponds to the post-reflected-shock condition for U_{is} = 3.55 km/s, P = 0.91 Torr, 2.2% CH_4/N_2, L = 10.16 cm. (Left) Raw detector signal. Measured transitions are indicated by dips in the measured absorbing signal. Time-zero is with respect to the passage of the incident shock. (Right) Sample absorbance versus relative wavenumber. Colored lines correspond to scans in time.

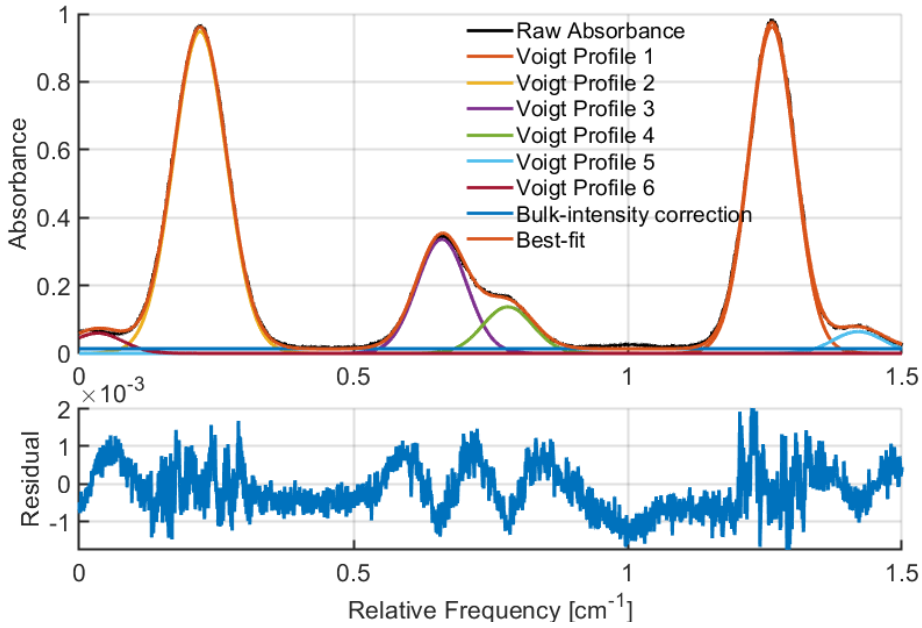

Fig. 5 Individual and overall best-fit Voigt profiles.

CN(X) most populated, followed by CN(A) and then CN(B). Assuming CN(Total) ≈ CN(X), it can be seen that the DPLR and TDLAS measurements are of the same order of magnitude but follow different trends. This is to be expected given differences in measured and predicted temperature.

The temperature and number density time-histories for a similar U_{is} and decreased P_{fill} at a 100 kHz scan rate is provided in Figure 7. Again, the experimental temperatures agree within 5-10%. There is also disagreement with the DPLR prediction at this condition, although the general trend is similar. Likewise, the trend in state populations is consistent between emission and TDLAS inferences, although DPLR predicts an increase of CN population at long test times which is opposite the measurement trend. As before, while DPLR and TDLAS measurements predict the same order of magnitude CN number density, the numbers do not agree quantitatively or in trend due to the significant

differences in temperatures.

Finally, the temperature and number density time-histories for a higher incident shock velocity condition at a 200 kHz scan rate is provided in Figure 8. As with the previous conditions, the emission-inferred and TDLAS-inferred temperatures trend together and agree within 5%, and with DPLR predictions within 10%. The CN(X) population time-history, as well, tracks DPLR predictions more closely than at the low-velocity conditions. Both experimental and simulated number density time-histories show a sharp increase in state population followed by a gradual decrease with time.

Overall, TDLAS and emission measurements for U_{is} = 3.61 and 4.86 km/s and P_{fill} = 0.91 and 0.4 Torr have been compared with DPLR predictions. At the lower temperatures, experimental measurements show average agreement on the order of 10%, following expected trends. While direct comparisons between state populations is not possible, the density of three electronic states are obtained and in future work may be used to examine the non-Boltzmann behavior of CN electronic states. DPLR predictions at low velocity show significant differences in the trends for temperature, CN formation and decay. At the higher temperature condition, both experimental and simulated temperatures agree well. The DPLR prediction of number density exhibits the same 40-50% decrease in population with time as the experimental inferences. The divergence at early test times between TDLAS-extracted CN(X) and DPLR CN(Total) for the lower velocity conditions may be attributed to a rapid production of CN that is not accurately captured in models, requiring further investigation into the CN kinetics mechanism. The discrepancy may also suggest experimental artifacts such as shock attenuation[20]. Limitations in the accuracy of modeling assumptions and replication of entry conditions continue to motivate the direct, quantitative measurement of thermochemical conditions produced by EAST.

VI. Conclusion

Measurements in 2.2% CH_4 in N_2 mixtures were taken in the incident post-shock region at the NASA Ames EAST facility for incident shock velocities ranging from 3.0-5.5 km/s and fill pressures between 0.3-1.15 Torr. Extracted Doppler temperatures exhibit a sharp jump after shock passage, decreasing gradually throughout the remainder of the test time. TDLAS and emission-inferred temperatures agree within 5%. However, there is an offset of approximately 20% between experimental measurements and DPLR predictions of temperature at lower velocity conditions. Similarly, the number density trends are consistent between TDLAS and emission inferences, although a direct comparison between each technique is not possible due to different CN electronic states being measured. Particularly interesting at lower velocity is a discrepancy in measured and simulated CN number density at early times. Measurements reveal a more rapid production of CN than anticipated by the model. While the discrepancy suggests likely inaccuracies in the chemical mechanism at low velocity, the applicability of the stagnation line similarity analysis requires further examination.

While there exists substantial literature on the spectroscopic properties of the CN Violet system, much less exists on the CN Red system. Hence, while this work serves to provide a complementary, quantitative characterization of EAST flows, these results serve also to inform additional investigation on the CN spectroscopic model. Future work for CN will utilize simultaneous measurements in the UV and near-IR to extract spectroscopic constants including broadening coefficients, and reaction rates to inform CN mechanisms.

VII. Future Work

Additional TDLAS measurements of post-shock non-equilibrium species in EAST are being pursued in a second test campaign targeting low-speed air. The LAS-based diagnostic for this campaign measures the fundamental NO band in the mid-infrared, near 1910, 1918 and 1943 cm^{-1}. This set of lines was optimized for strength, spectral isolation, and spread of lower vibrational and rotational quantum number, v" = 0-3 and J" = 9.5-58.5, respectively. To reduce the uncertainty in lineshape fitting and extracted quantities, each laser is set to scan over multiple features at 1 MHz scan rates. Additional lasers targeting 777 nm, 868 nm and 926.6 nm for excited oxygen and nitrogen will be employed for sufficiently high-temperature conditions. Overall, it is expected that these fast-scanning LAS-based diagnostics will yield high-quality, high-SNR measurements of mode-specific temperatures and species concentration profiles for a variety of test conditions and gas compositions. This will complement existing emission diagnostics in the EAST facility. A sensitive probing of the state-specific species will provide inferences of multiple temperatures and concentration profiles behind incident shocks, as well as relevant rates for non-equilibrium processes. These results may then be incorporated into existing flow and performance models, also informing radiation models. A second test series is also planned for the EAST Low Density Shock Tube (LDST) which will probe a lower density range of Titan entry with a

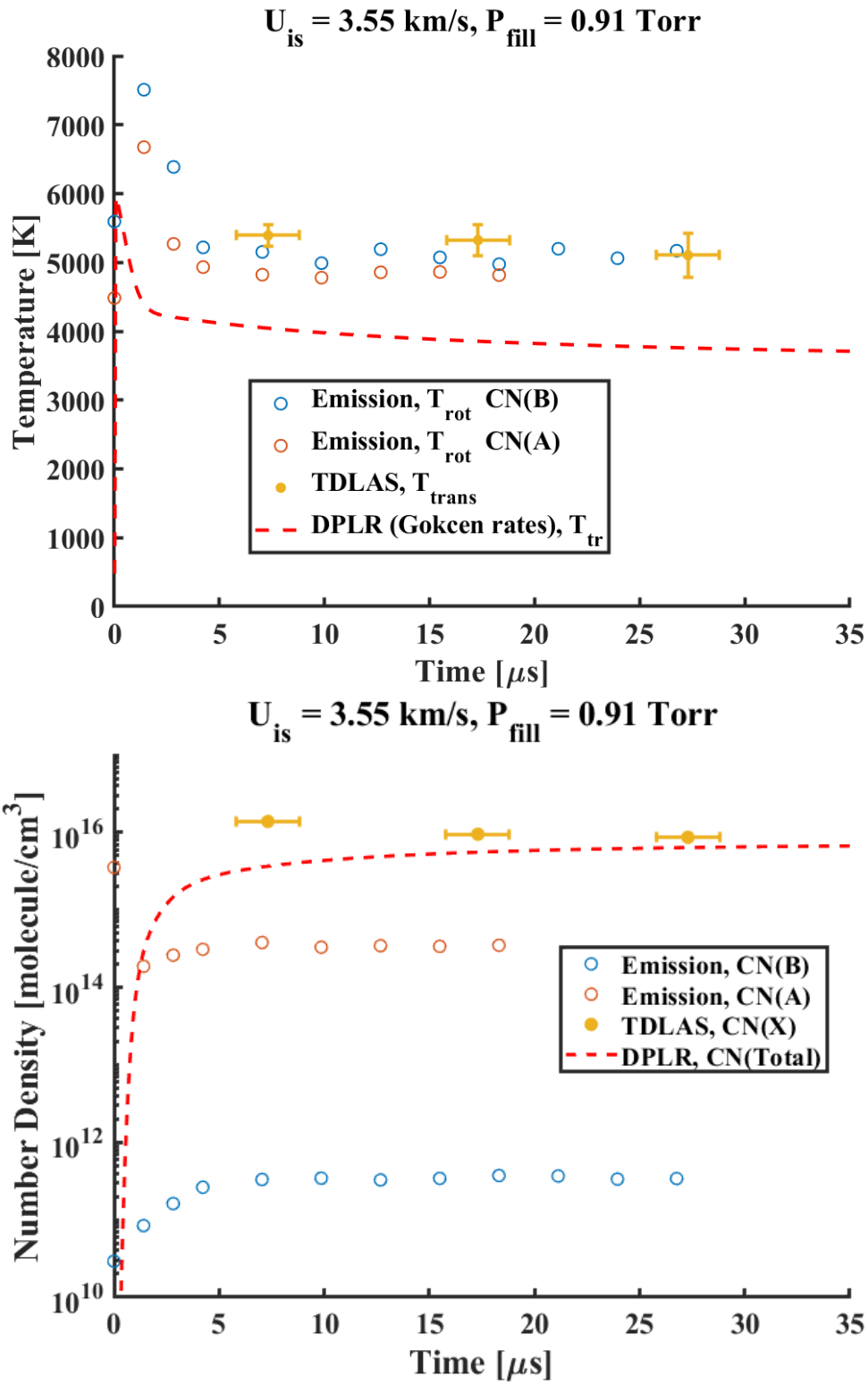

Fig. 6 (Top) Temperature and (Bottom) Number density time-histories for U_{is} = 3.55 km/s, P_{fill} = 0.91 Torr.

longer pathlength shock tube.

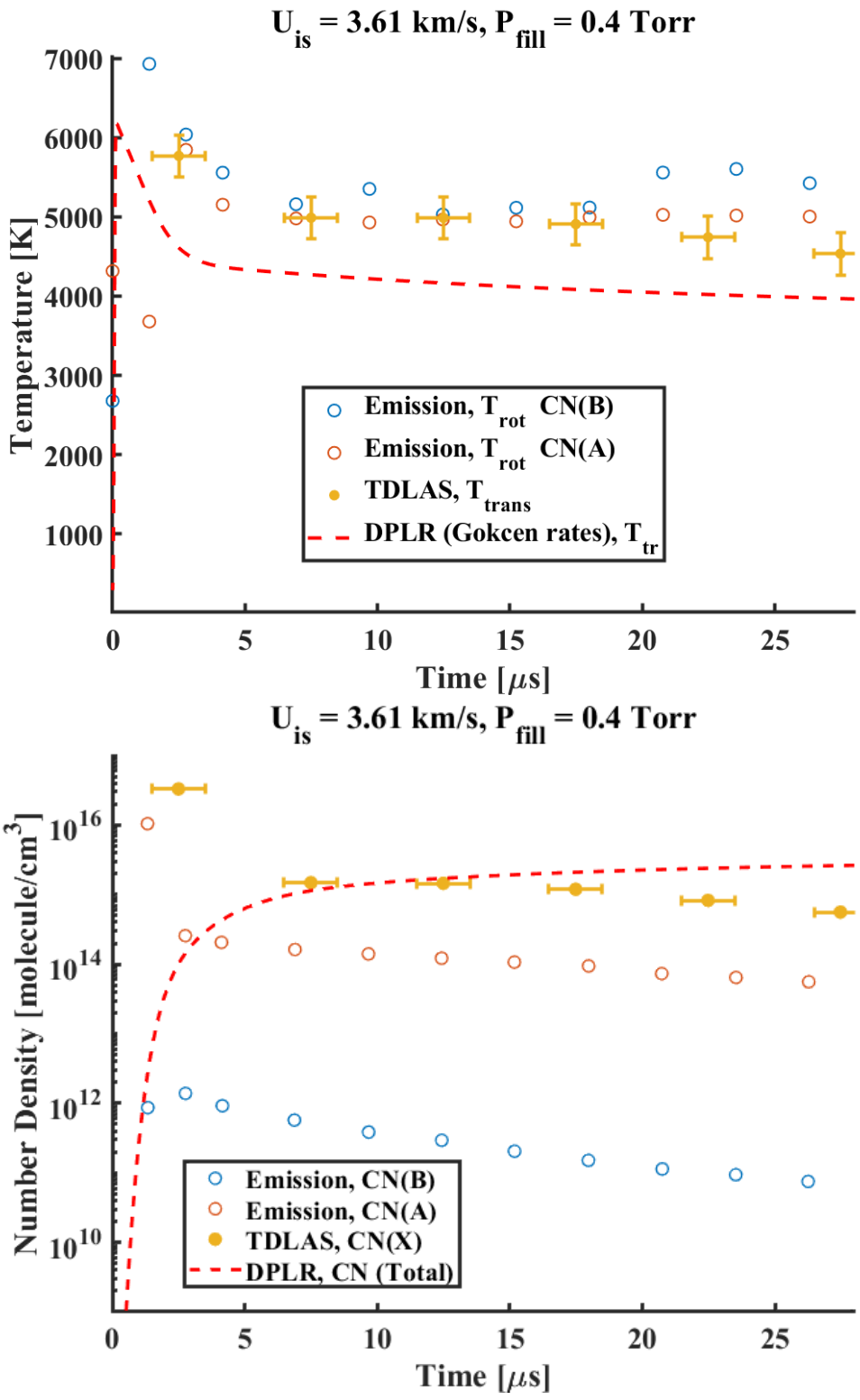

Fig. 7 (Top) Temperature and (Bottom) Number density time-histories for U_{is} = 3.61 km/s, P_{fill} = 0.4 Torr.

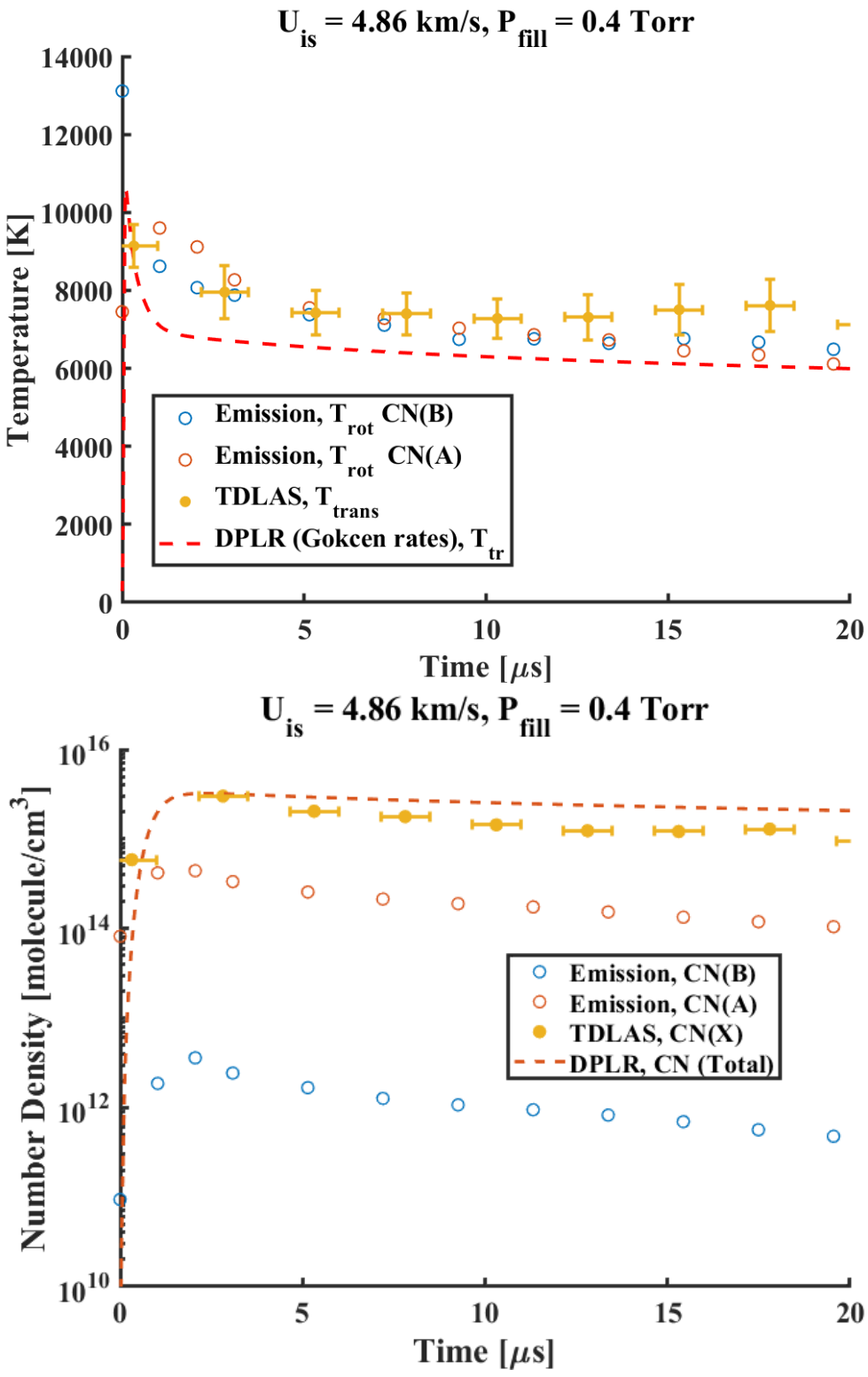

Fig. 8 (Top) Temperature and (Bottom) Number density time-histories for U_{is} = 4.86 km/s, P_{fill} = 0.4 Torr.

VIII. Acknowledgements

Efaine Chang is supported by a NASA Space Technology Research Fellowship. Augustin Tibere-Inglesse is supported by an appointment to the NASA Postdoctoral Program at the NASA Ames Research Center, administered by Oak Ridge Associated Universities under contract with NASA. Brett Cruden is supported by NASA contract NNA15BB15C to Analytical Mechanical Associates, Inc. This test campaign was supported by the Entry Systems Modeling project.

References

[1] Hank, J., Murphy, J., and Mutzman, R., "The X-51A Scramjet Engine Flight Demonstration Program," 15th AIAA International Space Planes and Hypersonic Systems and Technologies Conference, No. May, 2008, pp. 1–13.

[2] Walker, S., Sherk, J., Shell, D., Schena, R., Bergmann, J., and Gladbach, J., "The DARPA/AF Falcon Program: The Hypersonic Technology Vehicle #2 (HTV-2) Flight Demonstration Phase," 15th AIAA International Space Planes and Hypersonic Systems and Technologies Conference, Vol. 2, No. May, 2008, pp. 1–9.

[3] Kimmel, R.L., and Adamczak, D., "Hypersonic International Flight Research and Experimentation (HIFiRE) Fundamental Science and Technology Development Strategy," May, 2008, pp. 1–11.

[4] Bose, D., McCorkle, E., Thompson, C., and Grinstead, J., "Analysis and Model Validation of Shock Layer Radiation in Air," 46th AIAA Aerospace Sciences Meeting and Exhibit, 2008.

[5] Nompelis, I., Candler, G., and Holden, M., "Computational Investigation of Hypersonic Viscous/Inviscid Interactions in High Enthalpy Flows," 36th AIAA Thermophysics Conference, 2003.

[6] Brandis, A., Cruden, B., Prabhu, D., Johnston, C., and Bose, D., "Uncertainty Analysis of NEQAIR and HARA Predictions of Air Radiation Measurements Obtained in the EAST Facility," 42nd AIAA Thermophysics Conference, 2011.

[7] Bose, D., Wright, M.J., Bogdanoff, D.W., Raiche, G.A., and Allen, G.A., "Modeling and Experimental Assessment of CN Radiation Behind a Strong Shock Wave," *Journal of Thermophysics and Heat Transfer*, 2006 20:2, 220-230.

[8] Grinstead, J.H., Wright, M.J., Bogdanoff, D.W., and Allen, G.A., "Shock Radiation Measurements for Mars Aerocapture Radiative Heating Analysis," *Journal of Thermophysics and Heat Transfer*, 2009 23:2, 249-255.

[9] Helber, B., Chazot, O., Magin, T., and Hubin, A., "Space and time-Resolved emission spectroscopy of carbon phenolic ablation in air and nitrogen plasmas," 44th AIAA Thermophysics Conference, 2013.

[10] Almodovar, C. A., Spearrin, F. M., and Hanson, R. K., "Two-Color Laser Absorption Near 5 um for Temperature and Nitric Oxide Sensing in High-Temperature Gases," *Journal of Quantitative Spectroscopy and Radiative Transfer*, 203:572–581, 2017.

[11] Hanson R.K., Spearrin, R.M., and Goldenstein, C.S., "Spectroscopy and Optical Diagnostics for Gases," Springer International Publishing, 2016.

[12] Rothman, L. S., Gordon, I. E., Barber, R. J., Dothe, H., Gamache, R. R., Goldman, A., Perevalov, V., Tashkun, S. A. and Tennyson, J., "HITEMP, the high-temperature molecular spectroscopic database", *Journal of Quantitative Spectroscopy & Radiative Transfer*, 111, 2139-2150, 2010.

[13] Syme A., McKemmish, L.K., "Full spectroscopic model and trihybrid experimental-perturbative-variational line list for CN," *Monthly Notices of the Royal Astronomical Society*, Volume 505, Issue 3, August 2021, Pages 4383–4395, https://doi.org/10.1093/mnras/stab1551.

[14] Davidson, D.F., "RGFROSH: A real gas frozen shock equation solver," Tech. rep., Mechanical Engineering Department, Stanford University, Stanford CA, 94305, 1995.

[15] Cruden, B. A., "Absolute radiation measurements in Earth and Mars entry conditions," RTO-EN-AVT-218, 2014.

[16] Johnston, C. O. "Evaluating Shock-Tube Informed Biases for Shock-Layer Radiative Heating Simulations," AIAA Aviation 2019 Forum, 2019. doi: 10.2514/6.2019-3259

[17] Wright, M.J., White, T., and Mangini, N., "Data Parallel Line Relaxation (DPLR) Code User Manual; Acadia – Version 4.01.1," NASA TM 2009-215388, Oct. 2009.

[18] Gokcen, T., "N2-CH4-Ar Chemical Kinetic Model for Simulations of Atmospheric Entry to Titan," Journal of Thermophysics and Heat Transfer. 21. 10.2514/6.2004-2469, 2004.

[19] Johnston, C.O., West, T.K., and Brandis, A.M., "Features of Afterbody Radiative Heating for Titan Entry," AIAA 2019-3010. AIAA Aviation 2019 Forum, June 2019.

[20] Collen, P.L., Di Mare, L., McGilvray, M., and Satchell, M., "Analysis of Shock Deceleration Effects on Radiation Experiments in the NASA Electric Arc Shock Tube," AIAA SciTech 2022 Forum, January 2022.